Probing Oxygen Reduction Reaction Kinetics of Sr-Doped LaMnO$_3$ Supported on Y$_2$O$_3$-Stabilized ZrO$_2$

EIS of Dense, Thin-Film Microelectrodes

G. J. la O', B. Yildiz,[a] S. McEuen, and Y. Shao-Horn[*,z]

Electrochemical Energy Laboratory, Massachusetts Institute of Technology, Cambridge, Massachusetts 02139, USA

Dense microelectrodes fabricated with well-defined microstructures and geometries using microelectronic fabrication techniques were studied using electrochemical impedance spectroscopy (EIS) to investigate the rate-limiting reaction step(s) for oxygen reduction reaction (ORR) on the La$_{0.8}$Sr$_{0.2}$MnO$_3$ (LSM)/8 mol % Y$_2$O$_3$-stabilized ZrO$_2$ (8YSZ) system. At least four distinct reaction processes were observed for ORR on LSM/8YSZ under ambient PO_2 and at intermediate temperatures, which have been assigned tentatively to: (*i*) ion transport in 8YSZ with an average activation energy of 1.16 ± 0.02 eV, (*ii*) a surface diffusion process on LSM with activation energy in the range from 1.34 to 1.65 ± 0.03 eV, (*iii*) at least one surface chemical process on LSM with activation energies in the range from 1.71 to 1.88 ± 0.02 eV and an average capacitance value of 3.4 × 10^{-4} F/cm^2, and (*iv*) a mixed bulk/three-phase boundary (TPB) charge transfer process with activation energies in the range from 2.42 ± 0.02 to 3.05 ± 0.03 eV and an average capacitance value of 3.2 × 10^{-3} F/cm^2. This study suggests that the overall ORR rate may be limited by mixed bulk/TPB charge transfer processes below 700°C and surface chemical reactions above 700°C. The ORR current contributions from the bulk oxide ion transport and TPB incorporation path was estimated by correlating microelectrode geometry to impedance data.
© 2007 The Electrochemical Society. [DOI: 10.1149/1.2508887] All rights reserved.

Conventional solid oxide fuel cells (SOFCs) that consist of La$_{0.8}$Sr$_{0.2}$MnO$_3$ (LSM) cathode, 8 mol % Y$_2$O$_3$-stabilized ZrO$_2$ (8YSZ) electrolyte, and nickel–8YSZ (Ni–8YSZ) anode typically operate at 800–1000°C for enhanced power and minimized resistance losses.[1] These conventional LSM/8YSZ/Ni–8YSZ cells have been shown to be robust and successfully operate continuously for several thousand hours.[2] However, due to the cost associated with materials requirements at high temperatures, bringing to market these technologically proven cells has been slow.[3] Lowering the operating temperature of SOFCs to ~600°C would allow the use of metallic components in the system and simplify gas seals, which could lead to system cost reduction and durability enhancement. Therefore, there have been intense efforts to reduce the operating temperature of conventional SOFCs.[4-6] However, the main barrier to acceptable SOFC performance at ~600°C has been the voltage losses at the LSM cathode where oxygen reduction reaction (ORR) occurs.[7] Understanding the rate-limiting reaction during ORR in LSM is essential to minimizing voltage losses at the cathode and will lead to the accelerated development of high performance SOFCs at intermediate temperatures.

Porous LSM electrodes.— A large number of ORR studies have focused on porous LSM electrodes using experimental techniques such as electrochemical impedance spectroscopy (EIS) and steady-state polarization.[8-26] EIS is a technique that, in theory, allows the separation of physical processes occurring on the electrode surface, bulk electrode, and at the electrode–electrolyte interface in the time domain. This technique has an advantage over conventional steady-state polarization experiments as processes at SOFC electrodes and electrolytes are often influenced by more than one rate-limiting reaction. Although numerous rate-limiting reactions have been identified on porous LSM electrodes in many previous studies using EIS, discrepancy exists in the rate-limiting reactions and associated activation energies, as shown in Table I. The activation energy for a specific reaction or process is, ideally, a constant value for a given material under a given set of conditions and oxygen environment. As shown in Table I, Siebert et al.[10] report a limiting reaction with an activation energy of 1.8 eV for a process attributed to adsorbed oxygen dissociation on LSM in the temperature range of

680–970°C. Van Herle et al.[11] also observe a limiting reaction from adsorbed oxygen dissociation in the temperature range of 700–900°C with, however, a higher activation energy of 2.11 eV. Murray et al.[16] and Chen et al.[25] report a limiting reaction with an activation energy of 1.61 eV for adsorption and desorption of oxygen molecules from 550 to 850°C and 1.63 eV for oxygen dissociation in conjunction with surface diffusion from 700 to 950°C, respectively. Similar inconsistencies can be noted by comparing the findings of the other studies listed in Table I. The rate-limiting reaction step for porous electrodes typically includes a surface process having activation energies in the range of 1.61–2.11 eV.[10,11,16,19,25]

The main disadvantage to porous LSM electrode studies is that the critical features controlling ORR, such as three-phase boundary (TPB) length, electrode surface area, electrode particle size, and electrode–electrolyte interface, are difficult to quantitatively measure and compare from study to study. As a result, the variation in the pore size, particle size, TPB length, and surface area of LSM porous electrodes can yield an inconsistent determination of rate-limiting reactions. The use of thin-film cathodes with well-defined microstructure and geometry can provide new insights and improve our understanding of physical processes associated with ORR on the LSM/8YSZ system.

Dense thin-film LSM electrodes/microelectrodes.— Dense LSM thin-film electrodes[11,18,27,28] and microelectrodes[29-35] that allow for quantitative analysis of cathode geometry for correlation to the ORR pathway have been used to study the kinetics of ORR. Endo et al.[27,28] reveal that the impedance of dense thin-film La$_{0.81}$Sr$_{0.19}$MnO$_3$ (with no TPB) at 700–900°C is proportional only to film thickness (from 100 to 3000 nm) and is not affected by P$_{O_2}$ (in the range from 1 to 10^{-3} atm), which indicates that ORR is controlled by transport of oxide ions through the bulk of LSM thin film. Van Herle et al.[11] and Ioroi et al.[18] also examine dense thin-film La$_{0.8}$Sr$_{0.2}$MnO$_3$ in the 3–5 μm range using EIS in the temperature range of 700–1000°C. They report bulk ion transport dominating the impedance response and reveal the presence of two additional surface processes, oxygen molecule dissociation and an unidentified surface reaction.

Brichzin et al.[31,32] have first used EIS to study the kinetics of ORR of dense La$_{0.8}$Sr$_{0.2}$MnO$_3$ microelectrodes supported on YSZ at ~800°C with a range of electrode diameters from 20 to 200 μm and two thickness values (100 and 250 nm). The overall impedance response (or electrode polarization resistance obtained from imped-

---

* Electrochemical Society Active Member.
a Present address: Argonne National Laboratory, Argonne, Illinois 60439, USA.
z E-mail: shaohorn@mit.edu

Table I. Summary of attributed oxygen reduction mechanism with corresponding activation energy and peak frequency from EIS studies on porous LSM/YSZ in the literature.

Attributed process	Activation energy (eV) [Temperature (°C)]	Resonant frequency (Hz)	References
Oxygen molecule dissociation	1.8 [680–970]	100–10	Siebert, 1995 (Ref. 10)
Oxygen molecule dissociation	2.11 [700–900]	10–1	Van Herle, 1996 (Ref. 11)
Oxygen adsorption and dissociation	1.61 ± 0.05 [550–850]	4000–3000	Murray, 1998 (Ref. 16)
Dissociative adsorption, transfer to TPB, and surface diffusion	~2 [800–1050]	10,000–0.1	Jorgensen, 2001 (Ref. 19)
Dissociation and surface diffusion	1.63–3.02 [700–900]	100–0.1	Jiang, 2002 (Ref. 23 and 24)
Dissociation and surface diffusion	1.61 [700–950]	10	Chen, 2003 (Ref. 25)

ance data) has been shown to vary proportionally with microelectrode area and thickness, which supports the dominance of ORR current via bulk oxygen ion transport in LSM. TPB lines present on the microelectrodes show a measurable effect on the overall impedance under anodic bias only.[31,32] In addition, Koep et al.[33] have recently examined the impedance on dense microelectrodes of $La_{0.8}Sr_{0.2}MnO_3$ supported on YSZ as a function of thickness (from ~100 to ~3000 nm), from which ORR current has been found to be dominated by oxide ion transport through the film at 700°C for microelectrode thickness less than ~360 nm.

With a dense thin-film microelectrode platform, chemical interactions between O_2 molecules and the cathode surface, transport on the surface and in the bulk, and charge transfer on the surface or interface could be investigated experimentally as a function of electrode geometry, the chemistry and microstructure of electrode and electrolyte materials, temperature, voltage, PO_2, and current and voltage treatments. Although initial microelectrode studies[29-35] have provided valuable insights into the mechanism for ORR on LSM/YSZ, many fundamental questions remain unanswered, such as to what extent the ORR current is carried via bulk oxygen ion transport or TPB pathway and how surface diffusion of oxygen influences ORR. In particular, understanding the characteristics of surface chemical reactions, TPB, and bulk pathways is critical to obtaining high-performance SOFCs at operating temperatures as low as 600°C. In this paper, we study the ORR using dense, patterned $La_{0.8}Sr_{0.2}MnO_3$ microelectrodes on thin-film 8YSZ supported by alumina (Al_2O_3) and silicon (Si) substrates in the temperature range of 790 to 570°C. The effect of substrate on the impedance response is examined and a marked difference in the high-frequency impedance response is observed between electronically semiconducting and insulating substrates. In addition, impedance data of LSM/YSZ supported on alumina are analyzed as a function of temperature and LSM microelectrode size, from which four distinct processes associated with oxygen reduction can be identified. Moreover, the rate-limiting reaction of ORR on LSM/YSZ and the current contribution from the TPB and bulk pathway are discussed in detail as a function of temperature.

Experimental

Preparation of patterned LSM microelectrodes on 8YSZ.— 8YSZ (Praxair Specialty Ceramics, USA) was initially sputtered on Al_2O_3 (MTI Crystal, USA) and Si single-crystal substrates using 5 in. diameter stoichiometric oxide targets for 3 h using 400 W power with Ar/O_2 atmospheres of 7.5:1. The deposited films were then annealed in air at 800°C for 3 h. $La_{0.8}Sr_{0.2}MnO_3$ was subsequently deposited on top of 8YSZ by sputtering from similar 5 in. diameter stoichiometric targets (Praxair Specialty Ceramics, USA) for 2 h using 300 W power with Ar/O_2 atmospheres of 7.5:1 and the substrate heated to temperatures around 550°C. LSM microelectrodes were then fabricated by the following process: (*i*) spin-

coating of positive photoresist (Shipley Microposit, USA) on LSM followed by photomask exposure with electrode features of 50, 100, 150, and 200 μm, (*ii*) photoresist developing, and (*iii*) immersion of the LSM film in hydrochloric acid (HCl) for ~3 min to remove excess LSM and create the square microelectrodes. The finished LSM microelectrodes consisted of 10–30 arrayed square sets of multiple samples. The trilayer films that consisted of as-deposited LSM microelectrodes, 8YSZ thin film, and Al_2O_3 or Si substrate were subsequently annealed in air at 800°C for 10 h before any electrochemical measurements were performed.

Platinum (Pt) counter electrodes with dimensions of ~50 μm × ~2 mm were positioned ~10 μm away from the LSM microelectrodes by photolithography and Pt sputtering. Negative photoresist (Clariant, Switzerland) was spin-coated on top of the annealed LSM microelectrodes, followed by photoresist exposure under photomask and photoresist developing to outline the Pt counter electrode areas. Pt was then sputtered on the developed photoresist for 20 min with 100 W power in pure argon atmosphere. Excess Pt was finally removed by photoresist liftoff using acetone. Further details on the fabrication and photolithography processing of the microelectrodes can be found in a previous study.[36] The completed trilayer films are referred to as $Al_2O_3/8YSZ/LSM$ and Si/8YSZ/LSM in the remainder of the paper.

Elemental and structural analyses.— Surface elemental analysis of the annealed films was performed using X-ray photoelectron spectroscopy (XPS) (from Kratos, USA) with a monochromatized aluminum X-ray source (Al Kα). X-ray diffraction (XRD) patterns of these samples were collected using a Rigaku Rotaflex X-ray diffractometer (Tokyo, Japan) with a copper rotating anode (Cu Kα) under the glancing-angle mode with an incident X-ray angle of 5°. A specially designed aluminum (Al) holder was used to hold thin-film trilayer systems for XRD analysis. A continuous scan rate of 0.25°/min from 25 to 75° of 2θ was used for all samples.

Microstructural characterization.— Microelectrode geometry and morphology was examined before and after EIS testing using optical microscopy and scanning electron microscopy (SEM). LSM film thickness and surface roughness was measured using atomic force microscopy (AFM) (Veeco, USA). In addition, grain structure of annealed and sputtered LSM and 8YSZ films was revealed by cross-sectional transmission electron microscopy (TEM) on a JEOL 2010 operating at 200 keV. Cross-sectional TEM samples were prepared by sectioning the thin-film trilayer into ~3 × ~6 mm strips. The strips were then epoxy-bonded (M-Bond, Vishay Micromeasurements) with the sputtered films oriented face-to-face, and glued strips were mechanically thinned and polished, followed by ion-milling, to achieve electron transparency.

EIS.— EIS measurements of annealed LSM microelectrodes were performed using a microprobe station (Karl Suss, Germany)
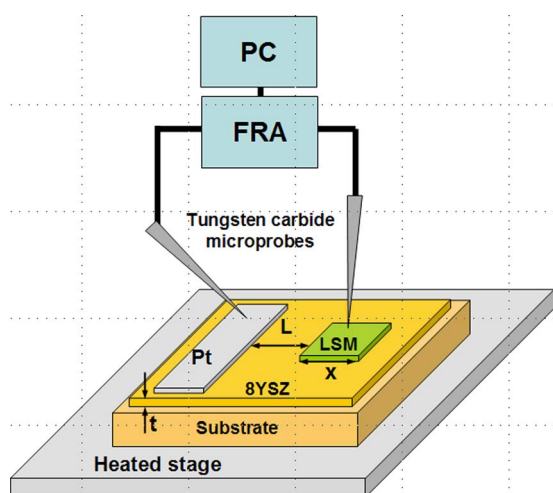
Figure 1. (Color online) EIS experimental setup for microelectrodes used in this study. The substrate/8YSZ/LSM-Pt trilayer samples were placed on a hot stage with Pt-coated tungsten carbide probe needles used for electrical contacts. Probe needles were connected to FRA and PC for data output.

Figure 2. (Color online) Optical micrograph showing the surface of LSM and Pt microelectrodes supported on Al_2O_3/8YSZ/LSM. The microelectrodes were found to be fully dense and crack free.

equipped with an optical microscope (Mitutoyo, Japan) and temperature-controlled stage (Linkam TS1500, U.K.), which was situated on a vibration isolation table. The LSM and Pt microelectrodes were electrically contacted using Pt-coated tungsten carbide probe needles with a 7 μm tip radius, which could be carefully positioned via micromanipulators. EIS measurements were conducted with a Solartron 1260 frequency response analyzer (FRA) connected to a Solartron 1296 dielectric interface in the frequency range from ~10 MHz to ~100 μHz using an ac voltage amplitude of 10 mV with zero dc bias. A schematic of the in-plane testing configuration and the two-electrode Pt–LSM cell is shown in Fig. 1. EIS tests were performed in ambient air atmosphere in the temperature range of 790–570°C with temperature intervals of 25–50°C. The actual sample temperatures were calibrated to the temperature-controlled stage using a thermocouple positioned on the YSZ film surface and this was observed to have a deviation of ±5°C for each temperature point measured. Four different microelectrode sizes were tested while the distance *L* between Pt and LSM electrodes was kept constant, as shown Fig. 1. Three EIS tests were performed at each temperature interval to ensure data reproducibility. In-plane electronic resistance of thin-film LSM microelectrodes can be significant, which has been shown by Koep et al.[33] for LSM electrodes with thickness lower than 180 nm. In this study, the EIS responses were found to be unchanged when the positions of microprobe needle contacts were varied on the LSM microelectrode, which suggested that in-plane electronic resistance of our LSM microelectrodes was insignificant. In addition, to clarify the influence of the Pt counter electrode on EIS data, identical Pt counter and working electrodes were tested and the impedance of these Pt–Pt cells were found to be less than 5% of the total LSM impedance at the largest working electrode size and highest temperatures tested, making the Pt counter electrode contributions negligible.

Results

Microelectrode structure.— The 8YSZ film and LSM microelectrodes were found to be fully dense and crack-free after annealing in both Al_2O_3/8YSZ/LSM and Si/8YSZ/LSM systems. A typical optical micrograph of Pt, annealed 8YSZ, and LSM surface in the Al_2O_3/8YSZ/LSM system is shown in Fig. 2. The microelectrodes showed no significant damage after EIS measurements with microprobe needles. AFM imaging of the 8YSZ and LSM surface revealed a fairly smooth surface with roughness in the range of 1–5 nm.
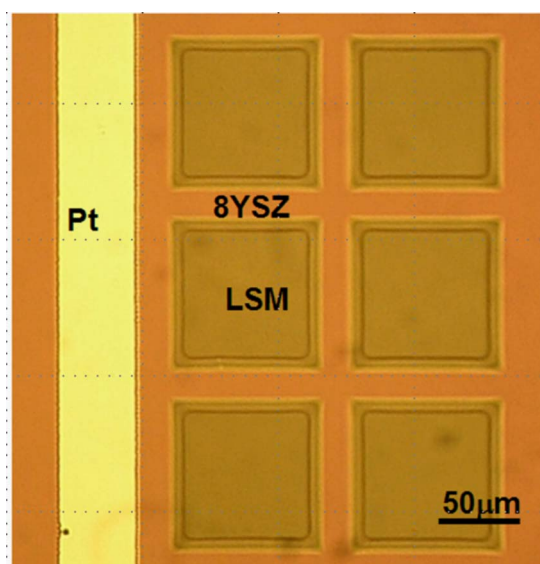
The thickness of 8YSZ film was measured to be 420 and 500 nm for the Al_2O_3/8YSZ/LSM and Si/8YSZ/LSM systems, as shown in Fig. 3a and b, respectively. Good adhesion of the electrolyte to the substrate layer was found for both samples. Cross-sectional TEM studies revealed that the grain structure of LSM and 8YSZ were columnar with grain widths in the range of 20–70 nm, as shown in Fig. 4a and b, respectively.
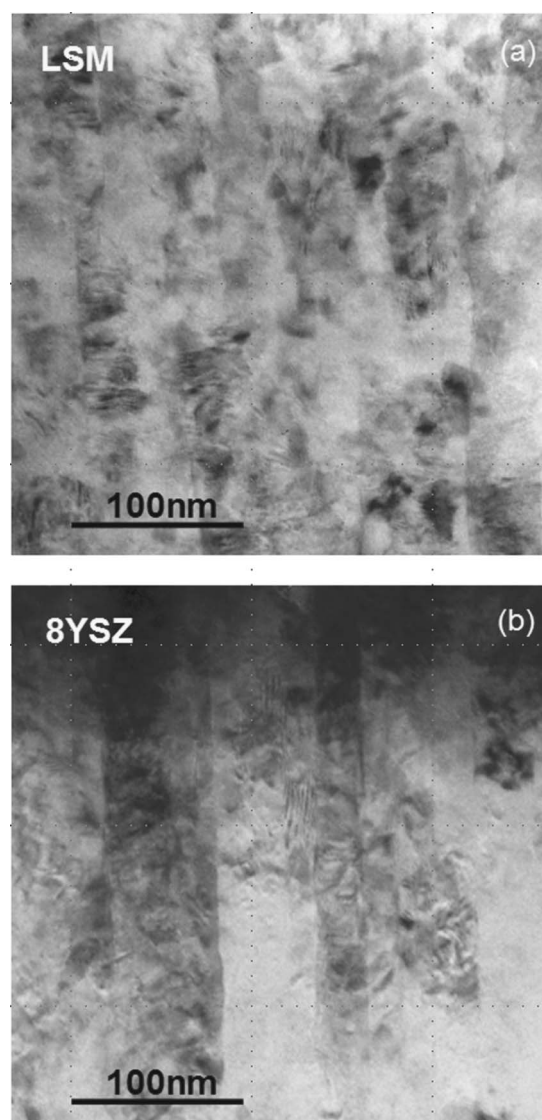
AFM measurements revealed that the thickness of the LSM microelectrodes was on the order of 240 nm for Al_2O_3 and 360 nm for Si substrate. In addition, the actual LSM microelectrode sizes were found to be smaller than ideal as a result of undercut etching, which resulted in sloping sidewalls, as shown in Fig. 5. In contrast, the Pt counter electrodes were found to have vertical sidewalls with geometries in good agreement with the photomask used. The actual LSM square sizes obtained in this study and thickness of the sputtered films are summarized in Table II.

Elemental and structural analysis.— XPS analyses show that the surface composition of Al_2O_3/8YSZ/LSM and Si/8YSZ/LSM samples could have lower manganese (Mn) content than ideal $La_{0.8}Sr_{0.2}MnO_{3-\delta}$ compositions. Considering $La_{1-x}Sr_xMnO_3$ ($x = 0.2$) as the ideal stoichiometry, the Sr and Mn contents in the Al_2O_3/8YSZ/LSM sample are 50 and ~30 atom % deficient, respectively. It has been documented in prior thin-film studies[37-39] that depositing LSM and similar perovskite materials such as $La_{1-x}Sr_xCoO_3$ (LSC) using radio frequency (rf)-sputtering techniques can result in nonstoichiometric A and B sites. The sputtered films were found to be crystalline and to have the perovskite structure after annealing. XRD patterns of the annealed 8YSZ/LSM films on Al_2O_3 and Si substrates are shown in Fig. 6a and b, respectively. XRD peaks from the Al sample holder are marked by arrows on the patterns. XRD peaks of the 8YSZ film were found to be in good agreement with those of the sputtering target and joint committee on powder diffraction standards (JCPDS).[40] However, the peaks of LSM in the Al_2O_3/8YSZ/LSM and Si/8YSZ/LSM were shifted slightly to higher 2θ values in comparison to those of stoichiometric $La_{0.8}Sr_{0.2}MnO_3$.[41] Arulraj et al.[42] have reported decreased lattice parameters in Mn-deficient films of $LaMn_{1-z}O_3$, where *z* ranges from 0 to 0.2. Therefore, both XRD and XPS measurements suggest that LSM microelectrodes in the Al_2O_3/8YSZ/LSM and Si/8YSZ/LSM samples are slightly Mn deficient.
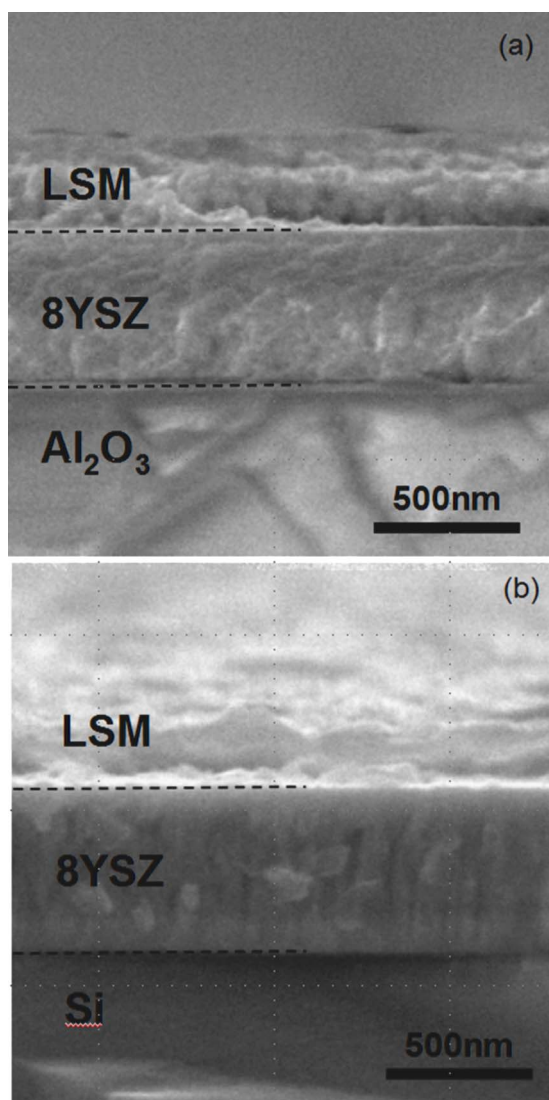
Figure 3. Cross-sectional SEM micrographs from (a) Al_2O_3/8YSZ/LSM and (b) Si/8YSZ/LSM showing dense 8YSZ film after annealing in air at 800°C for 10 h. The 8YSZ films are found well-adhered to the substrates


Figure 4. Cross-sectional TEM micrographs showing typical columnar grain morphology in (a) LSM and (b) 8YSZ sputtered films on Si/8YSZ/LSM after annealing in air at 800°C for 10 h. The columnar grains had widths of ~25 nm and lengths approaching the thickness of the film.

It is well known that lower Sr contents in LSM can reduce the electronic conductivity of the material; however, the decrease in the electronic conductivity from $La_{0.6}Sr_{0.4}MnO_{3-d}$ to $LaMnO_{3-d}$ has shown to be less than an order of magnitude[43] at ~600°C and above. Therefore, it is believed that the electronic conductivities of our Sr-deficient LSM microelectrodes may be similar to $La_{1-x}Sr_xMnO_3$ ($x = 0.2$). Although lowering the Sr content in $La_{1-x}Sr_xMnO_3$ from $x = 0.5$ to $x = 0.25$ reduces oxygen vacancy concentrations, this trend is not observed at low levels of Sr substitution.[44] In contrast, increasing Sr from $LaMnO_{3-d}$ to $La_{0.8}Sr_{0.2}MnO_{3-d}$ leads to a minor decrease in the vacancy concentration, diffusion coefficient of oxygen ions, and surface oxygen exchange coefficient.[44] Therefore, we believe that the effect of Sr deficiency in our thin-film samples on the ORR kinetics is not significant. As for Mn deficiency, a study by Mitterdorfer and Gauckler[12] has shown that there is no discernible change in the electrical conductivity between LSM$_{0.98}$ and LSMn$_{1.02}$. However, reduced Mn contents were found to be more susceptible to the formation of insulating phases (i.e., $La_2Zr_2O_7$) along the LSM/YSZ interface,[12] which could significantly alter ORR kinetics. No insulating phase was observed from cross-sectional TEM examinations of our thin-film samples after high-temperature annealing. As no

study that examines the effect of Mn stoichiometry on the kinetics of surface exchange and oxygen diffusion has been noted in the literature, it is assumed in this study that the extent of Mn deficiency in our thin-film samples has negligible effects on the rates of these two processes. Therefore, it is believed that the effect of Mn deficiency on our sputter deposited films on the ORR kinetics is not significant.

Effect of substrate.— EIS data obtained from in-plane measurements of the Al_2O_3/8YSZ/LSM samples are shown in Fig. 7, where a clear high-frequency intercept can be noted. Two additional high-frequency semicircle arcs other than a high-frequency intercept were observed for the Si/8YSZ/LSM system (Fig. 7a and 8), which could not be attributed to any electrochemical process given the testing geometry. Similar high-frequency behavior was also reported by Bieberle–Hutter et al.[38] using Si substrate, and this was attributed to electrical leakage.[38] Therefore, we speculate that the high-frequency semicircles from the Si substrate result from similar electrical leakage current or stray capacitance. A difference in impedance response between Si and Al_2O_3 substrates can be clearly noticed above 100 Hz in the plot of frequency (Hz) vs imaginary impedance ($-Z_{im}$), and the EIS data are identical for both systems at frequen-
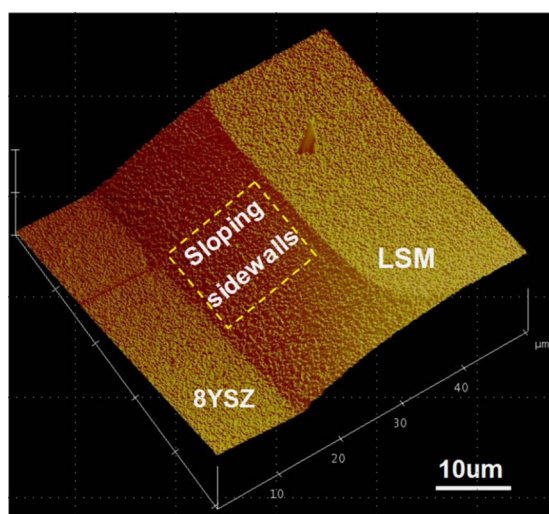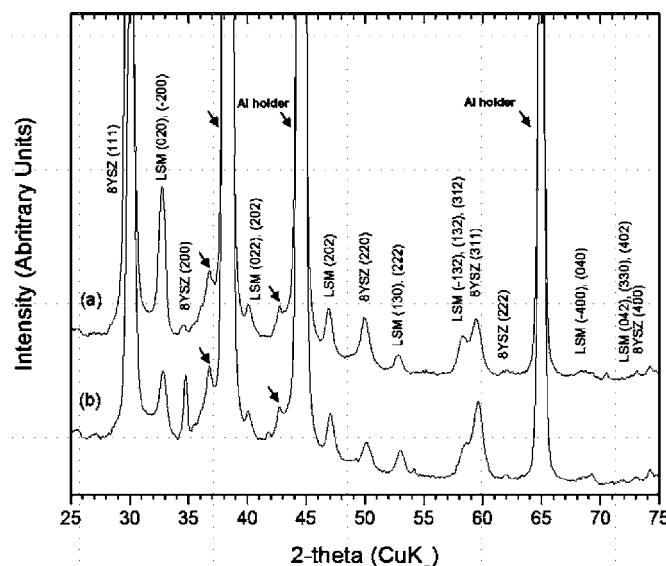
Figure 5. (Color online) AFM image of LSM microelectrode on Si/8YSZ/LSM that shows sloped LSM sidewalls due to undercut from acid etching during photolithography processing.

Figure 6. XRD patterns of sputtered (a) Al$_2$O$_3$/8YSZ/LSM and (b) Si/8YSZ/LSM films after annealing in air at 800°C for 10 h. X-ray patterns were collected using the glancing-angle mode with an incident angle of 5° and a 0.25°/min scan rate. Characteristic peak shift to higher 2θ is observed for the LSM film.

cies lower than 100 Hz, as shown in Fig. 8. High-frequency intercepts were always found for systems with electronically insulating substrates such as Al$_2$O$_3$, magnesia (MgO) and single-crystal 8YSZ. Our in-plane microelectrode studies show that the choice of substrates plays an important role in the impedance response of the electrodes of interest. As a result, subsequent EIS analyses in this paper are only focused on the electronically insulating Al$_2$O$_3$/8YSZ/LSM system.

Effect of temperature.— One large and depressed semicircle arc was found in the low-frequency range at temperatures above 700°C, which is labeled as LF in Fig. 7b for the Al$_2$O$_3$/8YSZ/LSM system. At temperatures lower than 700°C, two distinct semicircle arcs, LF1 and LF2, were revealed in the low-frequency range, as shown in Fig. 7c. These two low-frequency arcs become more apparent at even lower temperatures, as shown in Fig. 7d at 570°C. As temperature is decreased, the magnitude and peak frequencies of the LF1 and LF2 processes are further displaced apart to make these features more apparent. Moreover, an almost 45° linear region, labeled ALO-W, was found for the Al$_2$O$_3$/8YSZ/LSM system at frequencies directly below the ALO-HF intercept, as shown in the inset of Fig. 7d.

Equivalent circuit modeling.— Equivalent circuit modeling was used to analyze impedance data and extract parameters relevant to physical processes responsible for the high-frequency intercept (ALO-HF), the linear impedance regime (ALO-W), and the low-
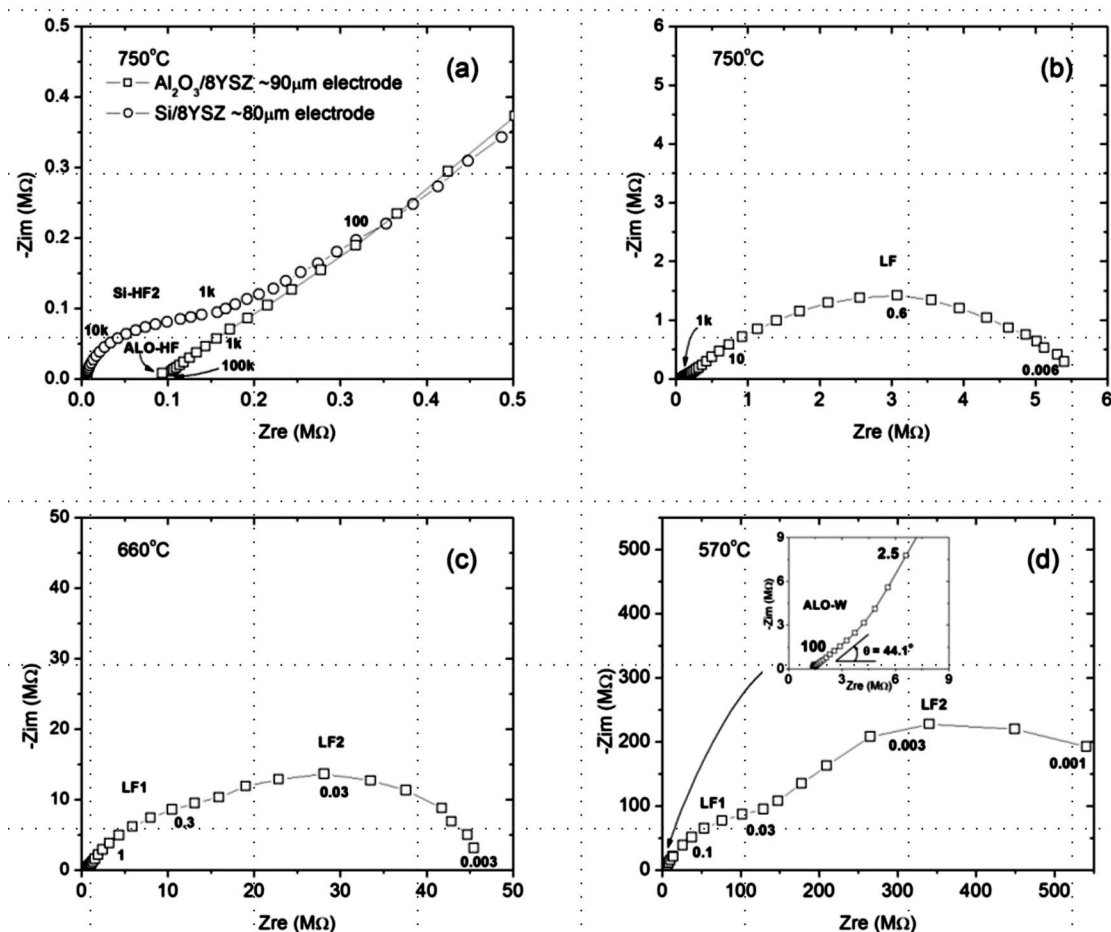
frequency arcs (LF1 and LF2). Mitterdorfer and Gauckler[12] had shown that the double-layer capacitance (C_{dl}) could mask the true faradaic impedance (Z_f) response of porous electrodes. The equivalent circuit used by Mitterdorfer and Gauckler[12] contains a resistance for the electrolyte (R_e) in series with a C_{dl} that is parallel to the Z_f component, which consists of the electrode impedance (Z_θ) and charge-transfer resistance (R_{ct}), as shown in Fig. 9a. We had tried to first subtract C_{dl} using the method developed by Berthier et al.[45] and apply this model in Fig. 9a to determine Z_f. Both C_{dl} and R_t were determined to be negligible in comparison to the electrode faradaic impedance. Therefore, an equivalent circuit with elements—R_e-W_1-(R_1/CPE_1)(R_2/CPE_2) shown in Fig. 9b was used instead to deconvolute the impedance response and extract resistance and capacitance values from the high-frequency intercept (ALO-HF), linear impedance region (ALO-W), and low-frequency semicircle arcs (LF1 and LF2). This alternative circuit contains an electrolyte resistance R_e that can be quantified from ALO-HF, in series with a finite-length Warburg element (W_1) that can be modeled from the linear regime ALO-W at high frequencies, and finally two sets of parallel resistance (R_1 and R_2) and constant phase elements (CPE_1 and CPE_2) to capture separate processes corresponding to LF1 and LF2 over the entire test-temperature range. Our experimental impedance features of ALO-W and LF1 as shown in Fig. 7d and inset do not bear the shape of Gerischer impedance and they cannot be modeled using one Gerischer-type impedance circuit element. Therefore, a separate finite-length Warburg (W_1) and one set of R-CPE elements (R_1 and CPE_1) have to be utilized.

High-frequency intercept ALO-HF.— The high-frequency intercept, ALO-HF, is plotted as a function of LSM size over the entire testing-temperature regime, as shown in Fig. 10a. An average slope of −1.01 ± 0.06 is observed for ALO-HF as a function of LSM square size. The activation energy of the high-frequency intercept ALO-HF for each microelectrode size was calculated using the relationship

Table II. Summary of ideal LSM electrode size, actual size obtained after photolithography, apparent TPB lengths, and sputtered film thickness on Al$_2$O$_3$/YSZ/LSM and Si/8YSZ/LSM systems.

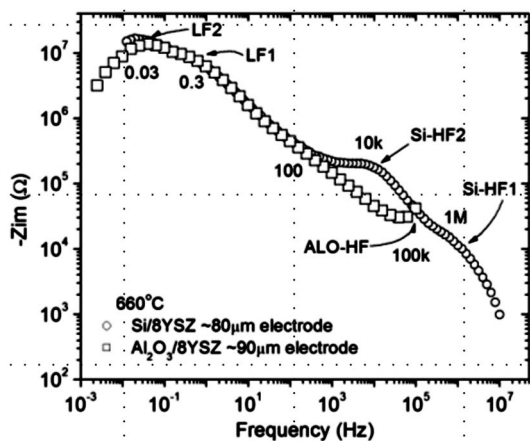|	Al$_2$O$_3$/8YSZ/LSM		Si/8YSZ/LSM	
Ideal square size (μm)	Actual square size (μm)	Apparent TPB length (μm)	Actual square size (μm)	Apparent TPB length (μm)
50	~40	~160	~40	~160
100	~90	~360	~80	~320
150	~140	~560	~130	~520
200	~190	~760	~180	~720
LSM Thickness	240 nm		360 nm	
8YSZ Thickness	420 nm		500 nm	

Figure 7. Nyquist plots from Al_2O_3/8YSZ/LSM $\sim$ 90 μm LSM electrode at (a) $\sim$750°C showing high frequency, (b) $\sim$750°C showing low frequency, (c) $\sim$660°C showing low-frequency, and (d) $\sim$570°C showing low-frequency areas with high-frequency inset. All tests conducted in air. Numbers in Nyquist plot are values of frequency in Hz.

$$G = \frac{G_0}{T} \exp\left(\frac{-E_a}{kT}\right) \qquad [1]$$

where the conductance G is equal to $1/R$ (unit of $1/\Omega$), T is the testing temperature in kelvin, and E_a is the activation energy in eV.


Figure 8. Log frequency vs log imaginary impedance (-Z_{im}) for Si/8YSZ/LSM $\sim$80 μm size and Al_2O_3/8YSZ/LSM $\sim$90 μm size LSM electrode at 660°C in air. Note the varied EIS response between the samples above 100 Hz frequency due to substrate effects and not from ORR on LSM.

The activation energy of ALO-HF was found independent of micro-electrode square size with an average of 1.16 ± 0.02 eV, as shown in Fig. 10b.

Linear impedance response ALO-W.— The finite-length War-burg element is used to quantify transport/diffusion processes in media of finite size. The finite-length Warburg element can be written as[46]
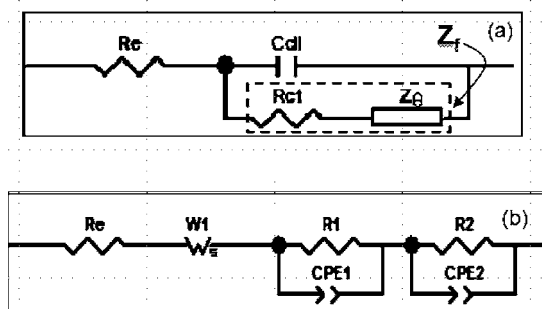
Figure 9. Equivalent circuit diagrams used with Al_2O_3/8YSZ/LSM EIS data for (a) subtracting double-layer capacitance (C_{dl}) to obtain the faradaic im-pedance (Z_f) and (b) quantifying resistance and capacitance values. R_e mod-els the high-frequency intercept ALO-HF, W1 is for the linear impedance region ALO-W, and R_i and CPE_i are used for semicircle arcs LF_i (where i = 1,2).
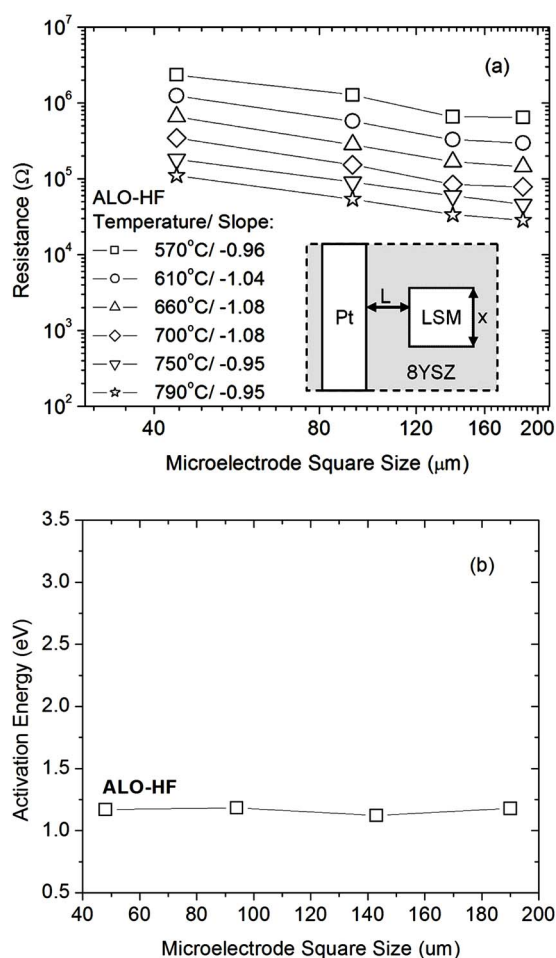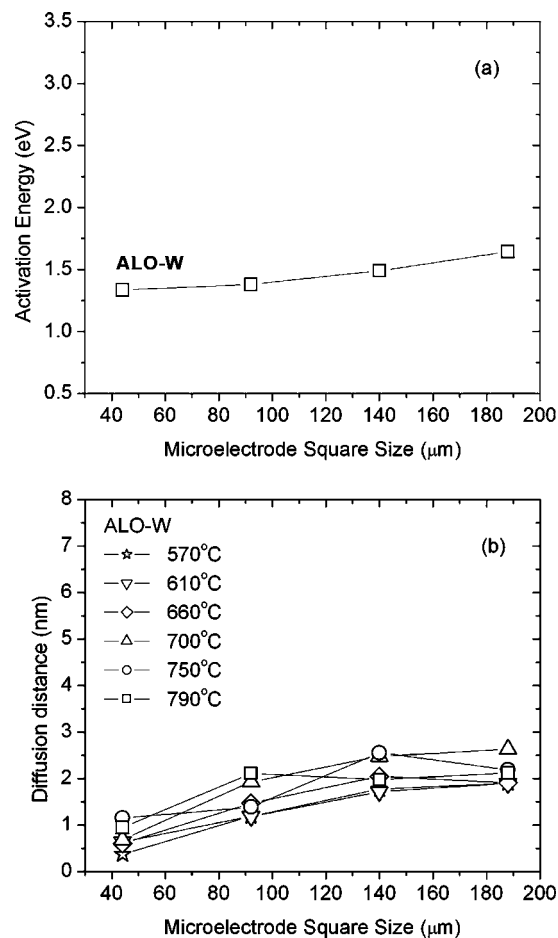
Figure 10. (a) High-frequency intercept ALO-HF in Al$_2$O$_3$/8YSZ/LSM system as a function of microelectrode size x (see inset of a) with constant Pt to LSM distance L ~ 10 μm and (b) activation energy for ALO-HF as a function LSM electrode size.

Figure 11. (a) Activation energy in Al$_2$O$_3$/8YSZ/LSM system for ALO-W diffusion resistance, R_w, from Eq. 2 as a function of LSM electrode size and (b) calculated diffusion length l as a function of microelectrode size at different temperatures from Eq. 7.

$$Z_w = R_w \frac{\tanh[(\tau i\omega)^\alpha]}{(\tau i\omega)^\alpha} \quad [2]$$

where Z_w is the Warburg impedance, R_w is the diffusion resistance in units of Ω, i is the imaginary number, τ is the characteristic time constant in seconds, and α is ideally 0.5. Using R_w obtained from equivalent circuit analysis of the model in Fig. 9b, the activation energies for ALO-W were calculated using Eq. 1. The activation energy of ALO-W was found in the range of 1.34 ± 0.05–1.65 ± 0.03 eV for different electrode sizes, as shown in Fig. 11a.

Low-frequency region LF1 and LF2.— As shown in the Nyquist plots for Al$_2$O$_3$/8YSZ/LSM in Fig. 7b, one large and depressed semicircle arc is observed above 700°C; however, this actually contains two semicircle arcs LF1 and LF2, as shown in Fig. 7d. The extracted real resistance associated with LF1 and LF2 for different microelectrode sizes are shown using Arrhenius plots in Fig. 12a and b, respectively. The activation energies for LF1 and LF2 were calculated using Eq. 1 which are shown as a function of microelectrode size in Fig. 13. The activation energies of LF1 (1.71–1.88 ± 0.02 eV) were found be consistently lower than those of LF2 (2.42 ± 0.02–3.05 ± 0.03 eV) for all microelectrode sizes. In addition, because the electrode geometries are known, a correlation between real impedance data (R_{LF1} and R_{LF2}) of LF1 and LF2 and microelectrode size can be made, as shown in Fig. 14a and b, respectively. Moreover, the sum of $R_{LF1} + R_{LF2}$ is plotted as a func-

tion of microelectrode size in Fig. 14c. The dependence of $R_{LF1} + R_{LF2}$ follows closely that of the R_{LF2} semicircle arc as this is typically 1 order of magnitude greater than R_{LF1}.

The capacitance values of LF1 and LF2 semicircles are shown in Fig. 15, which were obtained using the relationship[47]

$$C = (R^{1-p}\Phi)^{1/p} \quad [3]$$

where R is the parallel resistance value in the equivalent circuit, Φ is the nonideal capacitance, and p is the nonideality factor used to fit the CPE. Both Φ and p can be determined from modeling the impedance of the CPE element using the following expression[46]

$$Z_{CPE} = \frac{1}{\Phi(i\omega)^P} \quad [4]$$

where i is the imaginary number, ω the angular frequency, and Φ and p are the same variables as in Eq. 3.

Discussion

High-frequency intercept ALO-HF.— Given the testing geometries used this microelectrode study, the oxygen ion transport in the electrolyte occurs in-plane of the 8YSZ thin-film, as detailed in Fig. 1. In this study, the values of ALO-HF can be correlated to microelectrode size using the following expression
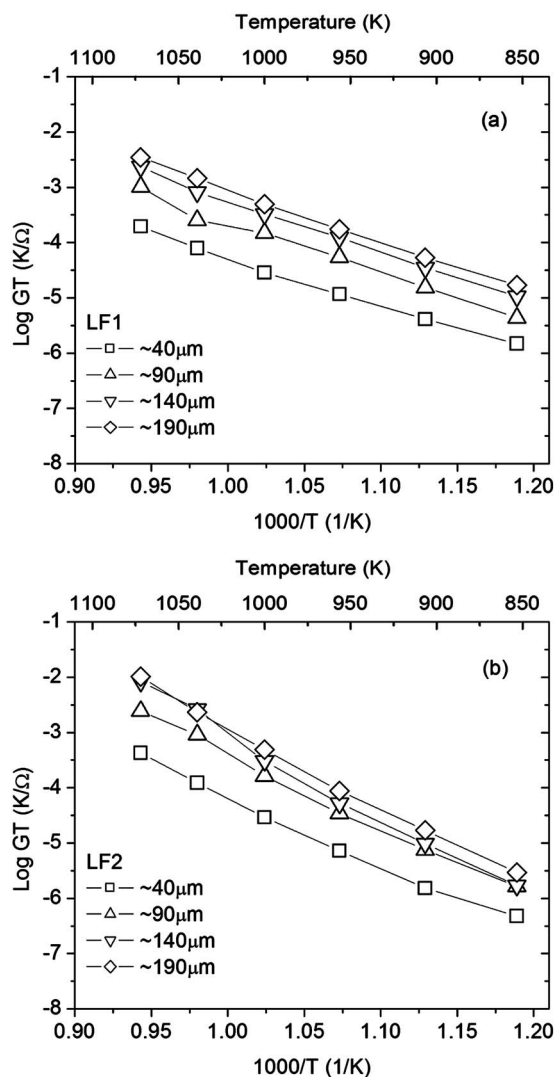
Figure 12. Arrhenius plot of real impedance (Z_{re}) as a function of temperature in Al_2O_3/8YSZ/LSM system for different LSM electrode sizes for (a) LF1 and (b) LF2 semicircle arcs.
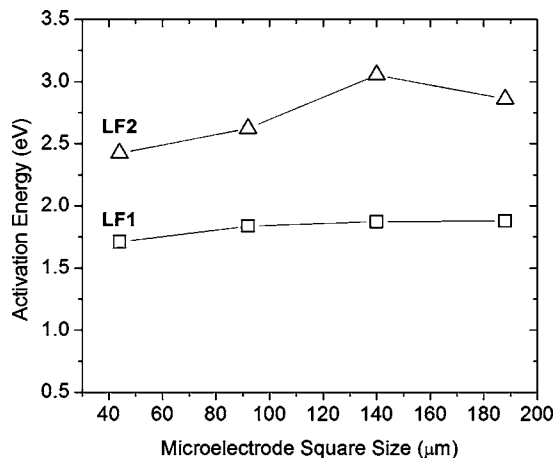

Figure 13. Activation energy as a function of LSM electrode size in Al_2O_3/8YSZ/LSM system for LF1 and LF2 semicircles over entire temperature range tested (570–790°C).
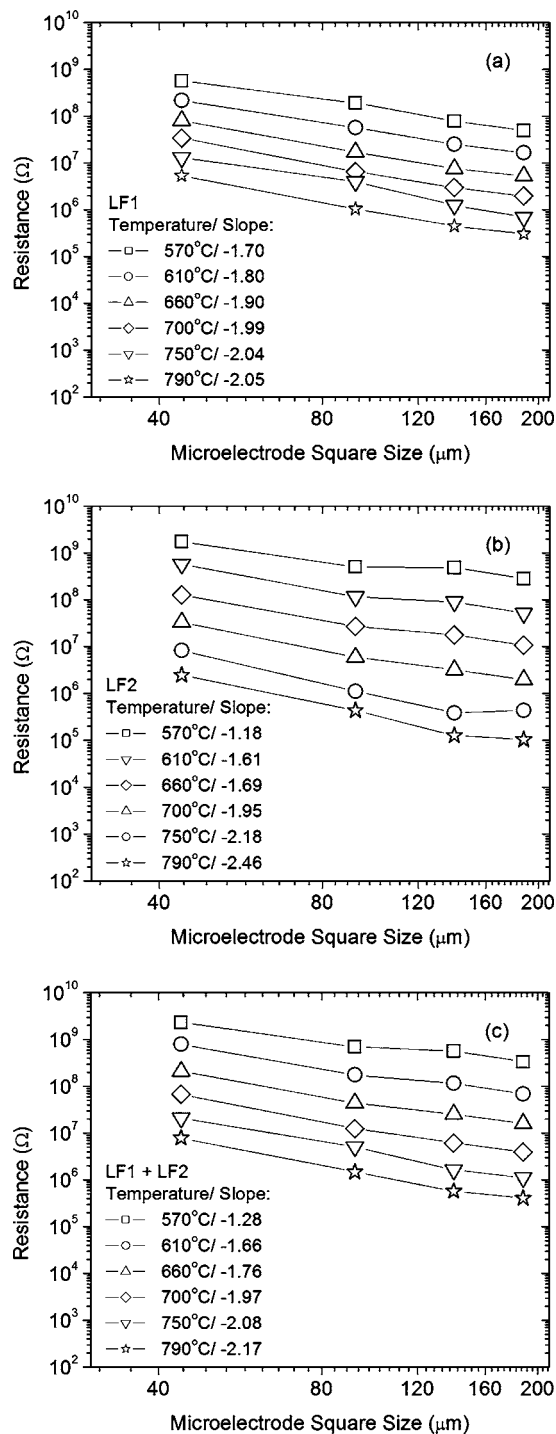
Figure 14. Real impedance (Z_{re}) as a function of LSM electrode size for (a) LF1, (b) LF2, and (c) LF1 + LF2 in the Al_2O_3/8YSZ/LSM system. Slope of -1 and -2 indicates TPB and surface/bulk/interface pathway dominance, respectively.

$$R_{8YSZ} = \frac{L}{\sigma_{8YSZ}tx} \qquad [5]$$

where L is the Pt to LSM distance, σ_{8YSZ} is the ionic conductivity of 8YSZ, t is the thickness of the 8YSZ film, and x is the LSM microelectrode square size (as shown in Fig. 10a inset). An average slope of -1.01 ± 0.06 was observed in the plot of ALO-HF as a function of microelectrode size x in Fig. 10a, which indicates that the ALO-HF intercept can be ascribed to oxygen ion transport in the
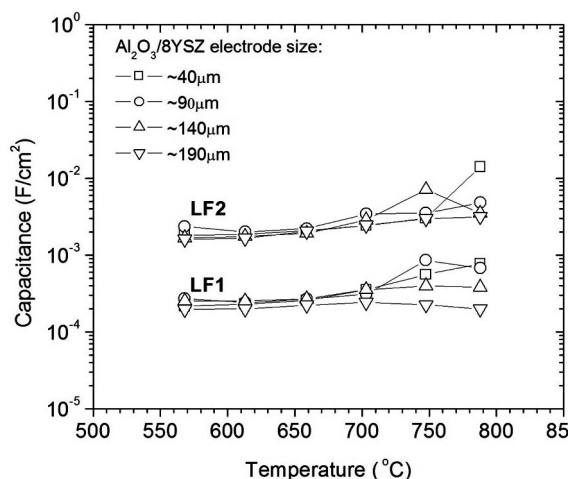
Figure 15. Capacitance as a function of temperature for LF1 and LF2 semi-circles in Al₂O₃/8YSZ/LSM system. An average capacitance of 3.4×10^{-4} and 3.2×10^{-3} F/cm² is observed for LF1 and LF2 arcs, respectively.

8YSZ film. Moreover, the reported values of activation energies for ion transport in 8YSZ range from 0.8 to 1.10 eV,[48-51] which is in close agreement with the average activation energy of 1.16 ± 0.02 eV obtained for ALO-HF in this study. It is important to mention that our in-plane testing configuration leads to nonuniformity in the current density along the 8YSZ electrolyte film and LSM microelectrodes, where the leading edges of the Pt and LSM microelectrodes have the lowest resistance to ion transport in 8YSZ. If most of the ion transport in 8YSZ occurred along the leading edge of LSM, a −1 slope dependence of ALO-HF on the LSM microelectrode size would be expected, which is observed experimentally in Fig. 10a.

Linear impedance response ALO-W.— Chen et al.[25] have reported that the activation energy for surface diffusion of oxygen in conjunction with adsorption on porous LSM electrodes is 1.61 eV. Lewis and Gomer,[52] on the other hand, using faceted Pt field emitters, report that the activation energy of oxygen surface diffusion on Pt is 1.45 eV above 500 K. Moreover, the surface of Pt is widely understood to be covered by oxide at temperatures above 527°C.[53-55] Therefore, it is speculated that similarities on the value of activation energy for oxygen surface diffusion on Pt and LSM might be attributed to the oxide coverage on both surfaces. Activation energies of ALO-W in the range from 1.34 ± 0.05 to 1.65 ± 0.03 eV were found for different electrode sizes (Fig. 11a), which might suggest that ALO-W might correspond to a surface diffusion process of oxygen species.

To verify whether ALO-W corresponds to the bulk diffusion of oxygen ions in LSM, we here estimate the bulk diffusion coefficients by assuming that R_w obtained from equivalent circuit analysis results from bulk diffusion in LSM using the following relationship

$$D_w = \frac{l}{R_w A} \frac{kT}{nq^2} \qquad [6]$$

where D_w is the bulk diffusion coefficient of oxygen ions (cm²/s), l is the characteristic diffusion length (the thickness of the film for bulk diffusion), A is the cross-sectional area for surface diffusion, n is the volume concentration of the mobile ion (#/cm³), q is the elementary charge, k is Boltzmann's constant, and T is the temperature (kelvin). The concentration of mobile ions vacancies, n, used for Eq. 6 was obtained from estimates by Van Hassel et al. of $\sim 5 \times 10^{15}$/cm³ at 1000°C.[56] Using the known microelectrode thickness and surface area in Table II for l and A, the calculated diffusion coefficients D_w were found to be ~ 7 to 10 orders of magnitude higher ($D_w^* \sim 10^{-6}$ cm²/s) than the reported bulk diffusivities

(3.10×10^{-16} to 1.6×10^{-13} cm²/s in the temperature range of 700–900°C) reported by De Souza et al.[57] This analysis shows the fact that R_w is too small in magnitude to result from bulk diffusion in LSM. The characteristic length l for surface diffusion of oxygen species might be estimated from the characteristic time constant τ (obtained from equivalent circuit analysis) using the relationship[46]

$$l = \sqrt{D\tau} \qquad [7]$$

where D is the surface diffusion coefficient in cm²/s. Although bulk diffusion coefficients of oxygen ions in LSM have been determined by De Souza et al.,[57] to the authors' knowledge, surface diffusion coefficients for LSM have not been reported. In the face-centered cubic metal systems, it has been reported that bulk diffusion is about 5 orders of magnitude smaller than surface diffusion.[58] For example, we may assume an oxygen surface diffusion coefficient of 1 $\times 10^{-11}$ cm²/s at 700°C and plot the characteristic diffusion distance calculated from Eq. 7 as a function of microelectrode size at different temperatures from the obtained activation energies, as shown in Fig. 11b. Just for comparison, the oxygen surface diffusion coefficient of 4.65×10^{-8} cm²/s on Pt at 800°C has been reported by Verkerk et al.[59] The characteristic diffusion length or utilization lengths were found to range from 0.5 to 3 nm and were not greatly affected by temperature. The small gradients in the oxygen ion concentration at the surface of LSM can, therefore, be explained by fast surface diffusion processes on LSM. Examination of activation energy, real impedance, and characteristic time τ extracted from the equivalent model based on the testing geometry does not support the assignment of the impedance feature to in-plane 8YSZ ionic current. Therefore, we tentatively assign the ALO-W feature to a surface diffusion process on LSM. Although the activation energy of ALO-W was found to slightly increase with increasing microelectrode sizes, the physical origin of this observation is not understood at this time.

Low-frequency region LF1 and LF2.— If the ORR rate-limiting reaction step were dominated by processes at the TPB, a relationship between TPB length and real impedance was first proposed by Kamata et al.,[14] which could be written as

$$R_{tpb} \propto \frac{1}{\sigma_e} \propto \frac{1}{L_{TPB}} \rightarrow R_{tpb} \propto x^{-1} \qquad [8]$$

where σ_e is the interfacial conductivity in S/cm², L_{TPB} is the total TPB length, and x is the microelectrode size that is equal to $\frac{1}{4}$ TPB length. In this case, a dependence of $R_{tpb} \propto x^{-1}$ or a slope of −1 is, therefore, expected. If the rate-limiting step of ORR were dominated by processes from the bulk (b), surface chemical reaction (s), and interface (int), the real impedance can be described by

$$R_{b/s/int} \propto x^{-2} \qquad [9]$$

In this case, a dependence of $R_{b/s/int} \propto x^{-2}$ or a slope of −2 is expected.

The observed dependence of LF1 on the microelectrode size in Fig. 14a is close to −2 throughout the temperature range tested, which indicates that this process is not dominated by oxygen reduction and incorporation of oxygen ions into the electrolyte at TPB. To further investigate and pinpoint the precise dominant process for LF1, the activation energies and capacitances of LF1 are examined. The activation energies of LF1 were found to vary in a small range of $1.71–1.88 \pm 0.02$ eV for the electrode sizes examined in this study, as shown in Fig. 13. Previous studies on porous electrode studies show that processes occurring on the electrode surface have activation energies in the range of 1.61–2.11 eV.[10,11,16,19,25] For example, Siebert et al.[10] and Van Herle et al.[11] have reported a rate-limiting step for ORR on porous electrodes involving oxygen dissociation having an activation energy of 1.8 and 2.11 eV, respectively. It is believed that the rate-limiting step responsible for LF1 originates from surface chemical processes. To further confirm that LF1 originates from surface chemical processes, the capacitance values for LF1 shown in Fig. 15 are compared with values found in the

literature. Adler[60] has recently reported that capacitance can be used as an indicator to determine the degree at which TPB or bulk participates in the reactions; capacitance values in the range of 1×10^{-5}–1×10^{-6} F/cm^2 are typically associated with oxygen reduction at TPB of the Pt/YSZ system. Although capacitance values are not reported in the study by Ioroi et al.[18] of thin-film LSM supported on chemical vapor deposited (CVD) thin-film YSZ, they could be estimated from the reported impedance data, where values of $\sim 10^{-4}$ and $\sim 10^{-3}$ F/cm^2 were obtained for the attributed surface and bulk processes, respectively. Moreover, Mitterdorfer and Gauckler[12] have reported a surface process on LSM/YSZ having capacitance values on the order of $\sim 10^{-4}$ F/cm^2, which have been attributed to competing dissociative adsorption and surface diffusion. Given the LF1 dependence on microelectrode size close to -2 (Fig. 14a), activation energies in the range of 1.71–1.88 ± 0.02 eV in this study (Fig. 13), and an average capacitance value of 3.4×10^{-4} F/cm^2 (Fig. 15), it is believed that surface chemical processes such as oxygen adsorption/desorption and dissociation are responsible for the LF1 semicircle. Although the activation energy of LF1 was also found to slightly rise with increasing microelectrode sizes, the physical origin of this observation is not understood at this time.

The LF2 semicircle, in contrast, has a slope dependence on the microelectrode size that ranges from -1.18 ± 0.08 at 570°C to -2.46 ± 0.07 at 790°C, as shown in Fig. 14b. Although the upper and lower limits for slope dependence are ideally -1 and -2, respectively, the slope values lower than -2 could be due to an experimental uncertainty as only four microelectrode sizes were used in the test. Slope dependence below -2 of ORR resistance as a function of electrode size has been found by Brichzin et al.[31,32] in a similar study on LSM microelectrodes at ~ 800°C. It is important to note, however, that the slope dependence on the electrode size clearly decreases and becomes more negative with increasing temperature. This change suggests that LF2 has a significant contribution from oxygen reduction and incorporation of oxygen ions into the electrolyte at TPB; the TPB pathway at low temperatures and shifts to a bulk dominated pathway at high temperatures (greater than ~ 700°C shown in Fig. 14b), where oxygen reduction and incorporation of oxygen ions into LSM occur on the LSM surface and oxygen ions diffuse in bulk LSM and migrate into the electrolyte. It has been previously reported using tracer diffusion measurements[57,61] that activation energies of 2.6–3.0 eV are related to bulk oxide ion transport processes in LSM. The range of activation energies found for LF2 from 2.42 ± 0.02 to 3.05 ± 0.03 eV is, therefore, in close agreement with these tracer diffusion studies. The activation energy rises with increasing electrode sizes, which might be attributed to a relatively greater contribution of bulk pathway to TPB pathway for larger electrode sizes. Moreover, Adler[60] and Kawada[62] have recently reported that capacitances found for the mixed ionic electronic conductor LSC approach 1×10^{-1} F/cm^2,[60,62,63] where oxygen reduction via the bulk pathway dominates. The observed capacitance values obtained for LF2 have an average of 3.2×10^{-3} F/cm^2, which is consistently 1 order of magnitude higher than that of LF1. Chemical capacitances of $\sim 10^{-3}$ F/cm^2 associated with oxygen reduction via bulk pathway in LSM can be estimated from the data published by Ioroi et al.[18] on dense thin films of LSM, which is in good agreement with the results found for LF2. Moreover, by assuming oxygen ion diffusion in bulk LSM is the rate-limiting step in the bulk pathway, the ionic conductivity for LSM can be estimated at temperatures higher than 700°C, where the bulk pathway is dominant. Using Eq. 5, average ionic conductivity values of 2.9×10^{-8}, 1.7×10^{-7}, and 5.2×10^{-7} S/cm were found at 700, 750, and 790°C, respectively. These values are in agreement with previously reported oxygen ion conductivities of $\sim 10^{-7}$ to $\sim 10^{-8}$ S/cm in LSM,[27,32,64] which confirms that oxygen reduction via bulk pathway is responsible for LF2 and bulk oxygen ion transport is the rate-limiting step in the bulk pathway above 700°C. Furthermore, our results are in agreement with the findings of Koep et al.[33] and Brichzin et al.,[31,32] in
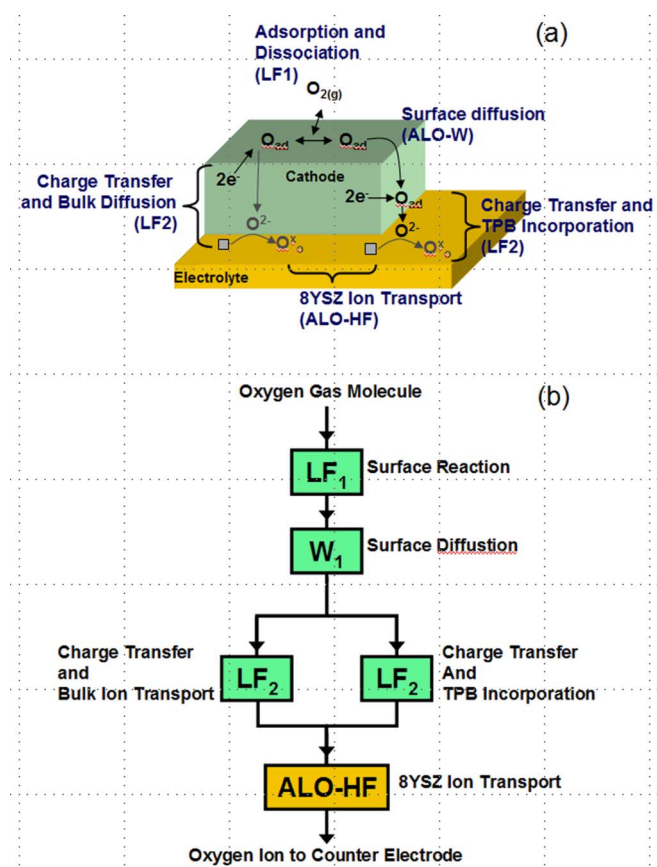

Figure 16. (Color online) Schematic of (a) the four ORR mechanisms observed in this study and (b) circuit diagram analog to the ORR process.

which the LSM bulk pathway is dominant and bulk oxygen ion transport is rate-limiting for ORR under similar temperatures and film thicknesses.

General Discussion and Conclusions

In this thin-film, dense microelectrode study, we clearly note four processes that take place upon oxygen reduction on LSM, which might be assigned tentatively to the following: (*i*) oxide ion transport in 8YSZ (ALO-HF) with an average activation energy of 1.16 ± 0.02 eV, (*ii*) surface diffusion on LSM (ALO-W) with activation energies in the range of 1.34 ± 0.05–1.65 ± 0.03 eV, (*iii*) surface processes on LSM (LF1) with activation energies in the range of 1.71–1.88 ± 0.02 eV and an average capacitance of 3.4×10^{-4} F/cm^2, and (*iv*) mixed charge transfer processes (LF2)—surface incorporation and bulk oxygen ion transport, and TPB incorporation changing as a function of temperature with activation energies in the range 2.42 ± 0.02–3.05 ± 0.03 eV and an average capacitance of 3.2×10^{-3} F/cm^2.

These four processes are illustrated on the LSM surface and at the LSM/YSZ interface and in a circuit diagram in Fig. 16a and b, respectively. It is proposed that at least two surface processes occur prior to the charge-transfer processes, which corresponds to surface chemical processes (LF1) and surface diffusion (ALO-W) on the LSM microelectrode. Although the exact nature of surface chemical reactions of LF1 has not been identified, our results are consistent with the hypothesis that surface oxygen adsorption and oxygen dissociation reactions are responsible for LF1. As shown in Fig. 16a and b, the surface chemical processes are then followed by two possible charge-transfer pathways into the 8YSZ electrolyte, either via the bulk of LSM or through the TPB. The real impedance of the four processes can be plotted as a function of temperature, and the results from the $\sim 190 \ \mu$m LSM microelectrode are shown in Fig.
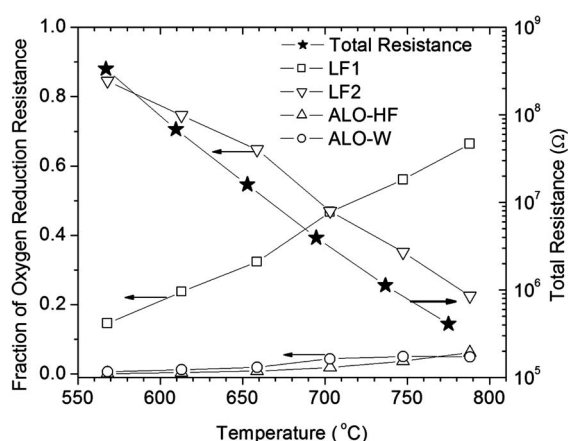
Figure 17. Plot of resistance fraction as a function of temperature for the ~190 μm LSM microelectrode. Below 700°C the LF2 semicircle arc is the rate-limiting reaction step due to largest resistance. Above 700°C the LF1 arc becomes the rate-limiting reaction step; however, the total resistance magnitude above 700°C is ~3 orders of magnitude smaller.

Figure 18. Plot of current path fraction as a function of temperature for the LF2 semicircle arc. Below 600°C the majority of ORR current passes through the TPB. Above 600°C, a significant fraction of current passes through the bulk of the LSM microelectrodes.

17. Assuming that a process with the largest fraction of total resistance would be the rate-limiting step of ORR, the mixed TPB/bulk charge-transfer process for LF2 limits ORR at temperatures lower than 700°C, and surface chemical processes become limiting above 700°C. The total real impedance at 570°C is approximately 3 orders of magnitude higher than at 790°C shown in Fig. 17, where surface rate-limiting ORR is observed. Therefore, the low polarization of LSM above 700°C observed for porous electrodes[1] having area specific resistance less than 0.5 Ωcm² can be attributed to reasonably fast TPB/bulk charge-transfer processes and surface chemical processes.
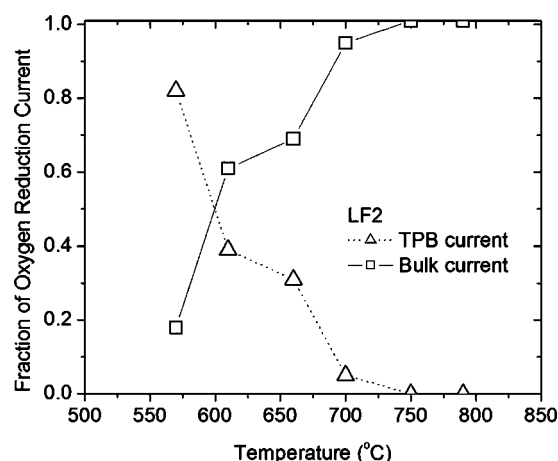
The change in the slope dependence on microelectrode size observed the LF2 semicircle was analyzed as a function of temperature, from which the fraction of oxygen ion current passing through the bulk and TPB pathways could be estimated by a first-order approximation. As previously mentioned, a slope dependence of −1 and −2 indicates a dominant TPB and bulk ionic pathway, respectively. For the slope dependence values between −1 and −2, the amount of current passing through the TPB or bulk can then be extracted using the expression below

$$\ln\left(\frac{A^{1-y}B^y}{C}\right) = (y-1)\ln\left(\frac{I_{TPB}}{I_{total}}\right) + y\ln\left(\frac{I_{bulk}}{I_{total}}\right) \quad [10]$$

where A, B, and C are pre-exponential factors determined from impedance data at the testing temperatures, y with values from 0 to 1 is the slope dependence of LF2 on microelectrode size, and I_x/I_{total} (x = TPB, bulk) is the fraction of the total current passing through the TPB and bulk paths. The derivation of Eq. 10 can be found in the Appendix. Given the scatter in the experimental data, all values smaller than −2 of slope in the range from 750 to 790°C is assumed to be −2. I_{TPB}/I_{total} and I_{bulk}/I_{total} from Eq. 10 is plotted as a function of temperature in Fig. 18. ORR current was found to be governed by the TPB charge-transfer pathway at temperatures below 600°C and to switch to the bulk path dominating above 600°C.

The in-plane geometries of the two-electrode Pt-LSM cell used in this study lead to nonuniform current densities along electrolyte and electrodes. Further experiments involving cross-plane geometries and three-electrode cells would provide further insights into the mechanism of ORR on LSM/YSZ and other cathode systems.

Insights into ORR kinetics from our microelectrode study could be potentially applied to guide the design and development of porous electrodes for low-temperature SOFCs. The TPB current in Fig. 18 is expected to dominate at even higher temperatures than 600°C as LSM particle aspect ratios in porous electrodes are closer to unity, originating from the larger surface area to bulk LSM rations. In addition, a similar effect of increasing TPB dominance would be observed when using thicker LSM films, as this would increase the bulk transport resistance and lead greater TPB current dominance. As the LF1 surface chemical reactions have much comparably smaller impedance than the LF2 process over a wide range of temperatures, decreasing particle sizes of LSM lead to lower ORR losses in SOFC cathodes due to a more facile surface pathway (Fig. 17). Porous electrodes with nanoparticles of LSM could, therefore, potentially provide much reduced polarization of ORR at operating temperatures as low as 600°C.

Using thin-film, patterned LSM microelectrodes, great versatility in probing the kinetics of ORR has been demonstrated by correlating the impedance response with the known electrode geometries. We note that the impedance response is highly dependent upon the substrate type used in the in-plane microelectrode measurements, and insulating substrates such as 8YSZ, MgO, or Al₂O₃ should be used to avoid the presence of artifacts at high frequencies. In addition, using in-plane configurations, a greater degree of current-density nonuniformity is present. At least four ORR processes are identified from the EIS measurements of LSM thin-film microelectrodes supported on 8YSZ with Al₂O₃ substrates, which have been assigned tentatively to (*i*) oxide ion transport in 8YSZ, (*ii*) a surface diffusion on LSM, (*iii*) at least one surface chemical process in LSM, with its precise nature to be determined by future EIS testing, and (*iv*) mixed bulk and TPB charge transfer in LSM. It is proposed that the overall ORR of LSM/YSZ microelectrodes is limited by the bulk/TPB charge transfer below 700°C, while the limiting reaction shifts to the surface chemical process(es) on LSM above 700°C. The ORR current contributions from the TPB and bulk pathways in these LSM microelectrodes have also been quantified, and ORR current from the bulk pathway appears to be dominant down to 600°C. Improved bulk properties and decreasing particle sizes are critical to reduce polarization in SOFCs to achieve high performance and efficiency at reduced temperatures below 600°C.

Appendix

Derivation of Eq. 10

$$\frac{1}{R_{\text{total}}} = \frac{1}{R_{\text{tpb}}} + \frac{1}{R_{\text{bulk}}}$$

$R_{\text{total}} = Cx^{-(1+y)}$ where x is the microelectrode square size

$$R_{\text{total}} = Cx^{\{-1+[-2-(-1)]y\}}$$

$$\ln\left(\frac{R_{\text{total}}}{C}\right) = \{-1+[-2-(-1)]y\}\ln x = \ln x^{-1} + y\ln x^{-2} - y\ln x^{-1}$$

$$\ln\left(\frac{R_{\text{total}}}{C}\right) = (1-y)\ln x^{-1} + y\ln x^{-2} \qquad \text{[A-1]}$$

at 750°C $R_{\text{bulk}} = Bx^{-2}$

$$\ln\left(\frac{R_{\text{bulk}}}{B}\right) = \ln x^{-2} \qquad \text{[A-2]}$$

at 570°C $R_{\text{tpb}} = Ax^{-1}$

$$\ln\left(\frac{R_{\text{tpb}}}{A}\right) = \ln x^{-1} \qquad \text{[A-3]}$$

plug in A-2 and A-3 into A-1

$$\ln\left(\frac{R_{\text{total}}}{C}\right) = (1-y)\ln\left(\frac{R_{\text{tpb}}}{A}\right) + y\ln\left(\frac{R_{\text{bulk}}}{B}\right)$$

$$\ln\left(\frac{A^{1-y}B^{y}}{C}\right) = (1-y)\ln\left(\frac{R_{\text{tpb}}}{R_{\text{total}}}\right) + y\ln\left(\frac{R_{\text{bulk}}}{R_{\text{total}}}\right)$$

because $R \propto \dfrac{1}{I}$

$$\ln\left(\frac{A^{1-y}B^{y}}{C}\right) = (1-y)\ln\left(\frac{I_{\text{tpb}}}{I_{\text{total}}}\right) + y\ln\left(\frac{I_{\text{bulk}}}{I_{\text{total}}}\right)$$

References

1. S. C. Singhal, *Solid State Ionics*, **135**, 305 (2000).
2. R. A. George, *J. Power Sources*, **86**, 134 (2000).
3. B. C. H. Steele, *J. Mater. Sci.*, **36**, 1053 (2001).
4. J. W. Fergus, *Mater. Sci. Eng., A*, **397**, 271 (2005).
5. Z. Zeng and K. Natesan, *Solid State Ionics*, **167**, 9 (2004).
6. S. P. Simner and J. W. Stevenson, *J. Power Sources*, **102**, 310 (2001).
7. S. C. Singhal and K. Kendall, *High-Temperature Solid Oxide Fuel Cells: Fundamentals, Design, and Applications*, Elsevier, New York (2003).
8. Y. Takeda, R. Kanno, M. Noda, Y. Tomida, and O. Yamamoto, *J. Electrochem. Soc.*, **134**, 2656 (1987).
9. B. Gharbage, T. Pagnier, and A. Hammou, *J. Electrochem. Soc.*, **141**, 2118 (1994).
10. E. Siebert, A. Hammouche, and M. Kleitz, *Electrochim. Acta*, **40**, 1741 (1995).
11. J. Van Herle, A. J. McEvoy, and K. R. Thampi, *Electrochim. Acta*, **41**, 1447 (1996).
12. A. Mitterdorfer and L. J. Gauckler, *Solid State Ionics*, **111**, 185 (1998).
13. A. Hammouche, E. Siebert, A. Hammou, M. Kleitz, and A. Caneiro, *J. Electrochem. Soc.*, **138**, 1212 (1991).
14. H. Kamata, A. Hosaka, J. Mizusaki, and H. Tagawa, *Solid State Ionics*, **106**, 237 (1998).
15. M. Odgaard and E. Skou, *Solid State Ionics*, **86-8**, 1217 (1996).
16. E. P. Murray, T. Tsai, and S. A. Barnett, *Solid State Ionics*, **110**, 235 (1998).
17. T. Ioroi, T. Hara, Y. Uchimoto, Z. Ogumi, and Z. Takehara, *J. Electrochem. Soc.*, **144**, 1362 (1997).
18. T. H. Ioroi, T. Y. Uchimoto, Z. Ogumi, and Z. Takehara, *J. Electrochem. Soc.*, **145**, 1999 (1998).
19. M. J. Jorgensen and M. Mogensen, *J. Electrochem. Soc.*, **148**, A433 (2001).
20. S. P. Jiang, J. G. Love, J. P. Zhang, M. Hoang, Y. Ramprakash, A. E. Hughes, and S. P. S. Badwal, *Solid State Ionics*, **121**, 1 (1999).
21. S. P. Jiang and J. G. Love, *Solid State Ionics*, **138**, 183 (2001).
22. S. P. Jiang, *J. Appl. Electrochem.*, **31**, 181 (2001).
23. S. P. Jiang, *Solid State Ionics*, **146**, 1 (2002).
24. S. P. Jiang, J. G. Love, and Y. Ramprakash, *J. Power Sources*, **110**, 201 (2002).
25. X. J. Chen, K. A. Khor, and S. H. Chan, *J. Power Sources*, **123**, 17 (2003).
26. J. D. Kim, G. D. Kim, J. W. Moon, Y. I. Park, W. H. Lee, K. Kobayashi, M. Nagai, and C. E. Kim, *Solid State Ionics*, **143**, 379 (2001).
27. A. Endo, M. Ihara, H. Komiyama, and K. Yamada, *Solid State Ionics* **86-8**, 1191 (1996).
28. A. Endo, H. Fukunaga, C. Wen, and K. Yamada, *Solid State Ionics*, **135**, 353 (2000).
29. T. Horita, K. Yamaji, M. Ishikawa, N. Sakai, H. Yokokawa, T. Kawada, and T. Kato, *J. Electrochem. Soc.*, **145**, 3196 (1998).
30. T. Horita, K. Yamaji, N. Sakai, Y. Xiong, T. Kato, H. Yokokawa, and T. Kawada, *J. Power Sources*, **106**, 224 (2002).
31. V. Brichzin, J. Fleig, H. U. Habermeier, and J. Maier, *Electrochem. Solid-State Lett.*, **3**, 403 (2000).
32. V. Brichzin, J. Fleig, H.-U. Habermeier, G. Cristiani, and J. Maier, *Solid State Ionics*, **152–153**, 499 (2002).
33. E. Koep, D. S. Mebane, R. Das, C. Compson, and M. Liu, *Electrochem. Solid-State Lett.*, **8**, A592 (2005).
34. E. Koep, C. Compson, M. Liu, and Z. Zhou, *Solid State Ionics*, **176**, 1 (2005).
35. R. Radhakrishnan, A. V. Virkar, and S. C. Singhal, *J. Electrochem. Soc.*, **152**, A210 (2005).
36. G. J. la O', B. Yildiz, and Y. Shao-Horn, Abstract 1499, The Electrochemical Society Meeting Abstracts, Vol. 2005-1, Quebec City, Canada, May 15-20, 2005.
37. A. Mineshige, M. Inaba, T. S. Yao, Z. Ogumi, K. Kikuchi, and M. Kawase, *J. Solid State Chem.*, **121**, 423 (1996).
38. A. Bieberle-Hutter and H. L. Tuller, in *MIT-Tohoku "21COE" Joint Workshop on Nano Science in Energy and Technology*, H. L. Tuller, A. Bieberle, T. Shoji, H. Yugami, H. Miura, and T. Kawada, Editors, Cambridge, MA (2004).
39. E. S. Vlakhov, R. A. Chakalov, R. I. Chakalova, K. A. Nenkov, K. Dorr, A. Handstein, and K.-H. Muller, *J. Appl. Phys.*, **83**, 2152 (1998).
40. O. A. Marina, C. Bagger, S. Primdahl, and M. Mogensen, *Solid State Ionics*, **123**, 199 (1999).
41. T. Hashimoto, N. Ishizawa, N. Mizutani, and M. Kato, *J. Cryst. Growth*, **84**, 207 (1987).
42. A. Arulraj, R. Mahesh, G. N. Subbanna, R. Mahendiran, A. K. Raychaudhuri, and C. N. R. Rao, *J. Solid State Chem.*, **127**, 87 (1996).
43. H. Kamata, Y. Yonemura, J. Mizusaki, H. Tagawa, K. Naraya, and T. Sasamoto, *J. Phys. Chem. Solids*, **56**, 943 (1995).
44. A. V. Berenov, J. L. MacManus-Driscoll, and J. A. Kilner, *Solid State Ionics*, **122**, 41 (1999).
45. F. Berthier, J. P. Diard, B. Legorrec, and C. Montella, *Corrosion (Houston)*, **51**, 105 (1995).
46. J. R. Macdonald, *Impedance Spectroscopy: Emphasizing Solid Materials and Systems*, Wiley, New York (1987).
47. J. Fleig, *Solid State Ionics*, **150**, 181 (2002).
48. J. E. Bauerle, *J. Phys. Chem. Solids*, **30**, 2657 (1969).
49. S. P. S. Badwal, *Solid State Ionics*, **52**, 23 (1992).
50. Y. Arachi, H. Sakai, O. Yamamoto, Y. Takeda, and N. Imanishai, *Solid State Ionics*, **121**, 133 (1999).
51. E. S. Thiele, L. S. Wang, T. O. Mason, and S. A. Barnett, *J. Vac. Sci. Technol. A*, **9**, 3054 (1991).
52. R. Lewis and R. Gomer, *Surf. Sci.*, **12**, 157 (1968).
53. J. L. Gland, *Surf. Sci.*, **93**, 487 (1980).
54. J. L. Gland, B. A. Sexton, and G. B. Fisher, *Surf. Sci.*, **95**, 587 (1980).
55. V. Stancovski, S. Sridhar, and U. B. Pal, *J. Electroceram.*, **3**, 279 (1999).
56. B. A. van Hassel, T. Kawada, N. Sakai, H. Yokokawa, and M. Dokiya, *Solid State Ionics*, **66**, 295 (1993).
57. R. A. De Souza, J. A. Kilner, and J. F. Walker, *Mater. Lett.*, **43**, 43 (2000).
58. N. A. Gjostein, *Short Circuit Diffusion*, American Society for Metals, Metals Park, OH (1973).
59. M. J. Verkerk, M. W. J. Hammink, and A. J. Burggraaf, *J. Electrochem. Soc.*, **130**, 78 (1983).
60. S. Adler, *Chem. Rev. (Washington, D.C.)*, **104**, 4971 (2004).
61. I. Yasuda, K. Ogasawara, M. Hishinuma, T. Kawada, and M. Dokiya, *Solid State Ionics*, **86-8**, 1197 (1996).
62. T. Kawada, J. Suzuki, M. Sase, A. Kaimai, K. Yashiro, Y. Nigara, J. Mizusaki, K. Kawamura, and H. Yugami, *J. Electrochem. Soc.*, **149**, E252 (2002).
63. S. B. Adler, *Solid State Ionics*, **111**, 125 (1998).
64. R. A. De Souza and J. A. Kilner, *Solid State Ionics*, **106**, 175 (1998).